



Thermal characterization and kinetic analysis of polyvinyl chloride containing Sn and Zn

Meng-yao Xue¹ · Yi-heng Lu¹ · Kang Li¹ · Bing Wang¹ · Yu-wei Lu²

Received: 22 January 2019 / Accepted: 12 June 2019 / Published online: 19 June 2019
© Akadémiai Kiadó, Budapest, Hungary 2019

Abstract

Polyvinyl chloride (PVC) films containing the mercaptan methyltin (S), zinc stearate (Z) and dipentaerythritol (D) additives were prepared. The thermal degradation kinetics of the films were investigated by nonisothermal thermogravimetry and TG–FTIR techniques. Using the nonmodel method and the Kissinger, the Friedman, the Kissinger–Akahira–Sunose and the Flynn–Wall–Ozawa methods, the average apparent activation energies of the PVC–SZD films in the first and second thermal decomposition stages obtained were 127.5 and 261.6 kJ mol⁻¹, respectively. Compared with the experimental master plot by the generalized master plot, the experimental and theoretical master plots on the master plot of $\theta/\theta_{0.5}$ versus α show that the thermal degradation of PVC–SZD film conforms to the chemical reaction F1.5 mechanism model. TG–FTIR analysis showed that the infrared vibration peaks ordered from strong to weak after adding SZD components were: ν_{CO_2} (638 °C) > $\nu_{(-\text{COOR})}$ (275 °C) > ν_{HCl} (299 °C). The thermal degradation of the film did not show hydroxyl or moisture formation compared to the blank. The removal of carboxyl groups of plasticizer dioctyl terephthalate (DOTP) in PVC was significantly inhibited, and the CO₂ gas released by thermal degradation was reduced by 85.2%. This suggests that SZD has a strong interaction with the ester groups in DOTP, and there is the possibility of generating a more stable carboxyl group-containing metal complex, which creates favorable conditions for the recovery of DOTP. When the heating rates were 2.5, 5.0, 10 and 20 °C min⁻¹, the lowest temperatures at which the conversions reached 5 and 10% were 226.1 °C and 239.1 °C, respectively.

Keywords Methyltin mercaptan · ZnSt₂ · Dipentaerythritol · Polyvinylchloride · Thermal degradation kinetics · TG–DTG–FTIR

Introduction

Polyvinyl chloride (PVC) and its products are important polymer materials with a global consumption of approximately 50 million tons [1]. Since the C–Cl bond energy is small at only 243 kJ mol⁻¹, it is usually necessary to add a heat stabilizer to suppress degradation in the molding process. Commonly used heat stabilizers thus far are composite lead salts, liquid metal soaps (Ba/Cd, Ba/Cd/Zn, Ba/Zn), complex calcium zinc, composite organotin, rare

earths metals and organic stabilizers, among which lead salts have tended to be phased out and banned due to their toxicity. The more widely used heat stabilizers are metal soaps, calcium zinc and organotins and are moving in a direction toward nontoxic, efficient and degradable stabilizers.

With the increasing consumption of organotin stabilizers in the processing of PVC products, the cost is reduced, the efficiency of use is improved, and the formation of composite stabilizers with calcium, zinc and rare earth metals, which are nontoxic and safe additives, has become a trend. The thermal degradation kinetics, environmental degradability and recycling economy of PVC products containing tin, calcium, zinc and other metals have attracted extensive attention.

The main research hotspots include the following: the thermal degradation of PVC, such as simultaneous catalytic

✉ Yi-heng Lu
yhlu@aust.edu.cn

¹ College of Chemical Engineering, Anhui University of Science and Technology, Huainan 232001, China

² Laboratoire de Chimie Physique, Université de Paris Sud, 91405 Orsay Cedex, France

degradation and dehydrochlorination, and the formation of chlorobenzene, which can be suppressed to the utmost in the presence of Ln_2O_3 and ZnO [2]; thermal dehydrochlorination kinetics of pure PVC under pyrolysis conditions [3]; TG–FTIR analysis of the thermal degradation of PVC and removal of HCl in the presence of Ca-based additives CaCO_3 , CaO and $\text{Ca}(\text{OH})_2$ [4]; TG–FTIR thermal degradation, pyrolysis behavior and kinetic analysis of typical plastics (including pure PVC resin) under a high heating rate [5]; morphological characteristics of dechlorination of polyvinyl chloride (PVC) during pyrolysis including the effects of PVC content and heating rate [6]; a pyrolysis gas produced from PE, PP, PS, PVC and PET alone and in a mixture [7]; the recycling of PVC waste [8]; TG/FTIR studies of the coprolysis behavior of PE/PVC/PS [9]; TG–FTIR and TG–EGA methods were used to study the thermal degradation of insulated PVC cables [10]; non-isothermal degradation kinetics of polyvinyl chloride/poly(ethylene oxide) blends [11]; thermal degradation kinetics of polyvinyl chloride, including thermogravimetric analysis and spectroscopy [12]; lifetime simulation and thermal characteristics of PVC cable insulation [13]; a kinetic model of pure polyvinyl chloride thermal dehydrochlorination [14]; a theoretical study on the thermal dehydrochlorination of polyvinyl chloride model compounds [15]; Raman and infrared spectroscopy used to study plasticizers in PVC films [16]; the effect of zinc borate and wood powder on thermal degradation and flame retardancy of PVC composites [17]; a thermogravimetric study of bioactive maleimide-based aromatic 1,3,4-oxadiazole derivative stabilizers for rigid PVC [18]; and thermal degradation of flame-retardant high-voltage cable sheathing (PVC) and insulating material (XLPE) by TG–FTIR [19].

Despite the large number of reports on the thermal degradation of PVC, there are few reports on the thermal degradation kinetics of polyvinyl chloride by representative additives such as methyltin mercaptan (S), zinc stearate (Z) and dipentaerythritol (D). These additives have entered the environment with the huge consumption of PVC products, and their stability, environmental degradability and recycling possibility are urgent problems that need to be solved. To clarify the thermal degradation process and mechanism of S, Z and D additives on PVC soft products, this work was performed based on our previous work studying the effects of organotin and barium stearate on the thermal stability of polyvinyl chloride [20, 21], and we used nonisothermal thermogravimetry, TG–FTIR and kinetic models with methyltin mercaptan (S), zinc stearate (Z) and dipentaerythritol (D) as additives to investigate the thermal degradation kinetics of a PVC film containing SZD components.

Using the Kissinger method, the Friedman method, the Kissinger–Akahira–Sunose (KAS) method, and the Flynn–Wall–Ozawa (FWO) method, the average apparent activation energies obtained for the thermal degradation of the PVC–SZD film in the first and second stages were 127.5 and 261.6 kJ mol^{-1} , respectively. Comparing the generalized master plots with the experimental master plots, on the curve of $\theta/\theta_{0.5}$ versus α , the experimental master plot and theoretical master plot of the chemical reaction F1.5 mechanism model are more consistent. This shows that the thermal degradation of the PVC film containing SZD conforms to the chemical reaction F1.5 mechanism model. The differential mechanism function $f(\alpha)$ is $2(1 - \alpha)^{3/2}$, and the integral mechanism function $g(\alpha)$ is $[1/(1 - \alpha)^{1/2}] - 1$.

When the heating rates were 2.5, 5.0, 10 and 20 $^\circ\text{C min}^{-1}$, the lowest temperatures at which the conversion reached 5 and 10% were 226.1 $^\circ\text{C}$ and 239.1 $^\circ\text{C}$, respectively. TG–IR analysis showed that the infrared vibration peaks from strong to weak with the addition of SZD in PVC were: ν_{CO_2} (638 $^\circ\text{C}$) > $\nu_{(-\text{COOR})}$ (275 $^\circ\text{C}$) > ν_{HCl} (299 $^\circ\text{C}$). The thermal degradation of the film showed no hydroxyl or moisture formation compared with the blank and significant inhibition of removal of carboxyl groups from the plasticizer dioctyl terephthalate (DOTP) in PVC, which reduced the CO_2 gas released due to thermal decomposition by 85.2%. This result suggests that SZD has a strong interaction with the ester groups in DOTP, and there is the possibility of generating a more stable carboxyl group-containing metal complex, which will provide favorable conditions for PVC soft products to recover DOTP.

Experimental

Materials

Industrial-qualified, Grade S-65 PVC resin (Q/NPVC01-2016) was supplied by the Formosa Plastics Industry (Ningbo) Co. Ltd., China; dioctyl terephthalate (DOTP) with 98.5% purity was obtained from the Bluesail Chemical Co. Ltd., China; industrial-qualified mercaptan methyltin (S), model DX-181, was supplied from the Quzhou Jianhua Dongxu Auxiliary Co. Ltd., China; industrial-qualified zinc stearate (Z), with a melting point of 118–125 $^\circ\text{C}$ and a zinc content of 10.5~11.5% was obtained from Zibo Luchuan Rubber & Plastics Additive Co. Ltd., China; 90%, analytically pure dipentaerythritol (D) was purchased from the Shanghai Maclean Biochemical Technology Co. Ltd., China.

TG–DTG analysis

TG analysis was performed using a thermogravimetric analyzer produced by the TA Instruments, model SDT2960. The investigation was performed at a flow rate of 50 mL min⁻¹ under nitrogen atmosphere, and 10–15 mg of each sample was heated from 25 to 700 °C with a heating rate β of 2.5, 5, 10 and 20 °C min⁻¹.

TG–FTTR analysis

TG–FTTR measurements were determined on a PerkinElmer TGA 8000 thermogravimetric analyzer coupled with a Frontier FTIR Spectrometer American PE FTIR spectrometer under a high-purity N₂ atmosphere with a heating rate of 10 °C min⁻¹ at a flow rate of 25 mL min⁻¹, and the FTTR spectra were recorded in the range of 400~4000 cm⁻¹.

Preparation of samples

The mixer model used is SU-70, which is produced by China Changzhou Suyan Technology Co., Ltd.; the tablet press is a flat vulcanizing machine, model 350 × 350, produced by Zhengzhou Xinhe Machinery Manufacturing Co., Ltd., China. First, PVC, DOTP, S, Z and D were measured, respectively, with the feed ratios of 100: 50: 0~1.0: 0~1.0:0~1.0 (phr). DOTP, S, Z and D were mixed first, followed by heating and dissolving. This mixture was then mixed with PVC at high speed at a temperature of 170–180 °C. The speed of rotation is 40 r min⁻¹ after mixing for 3~5 min when the torque reached a minimum value and then increased rapidly for approximately 0.5 min, followed by shut down, pressing into a sheet at 100 °C and removal. PVC samples (1 mm thickness) containing P-S, P-SZ and P-SZD were obtained as shown in Table 1.

Under high-purity argon atmosphere, TG–FTIR was used to heat up to 700 °C from a temperature rise rate of 10 °C min⁻¹ at 25 °C to measure the released gas by FTIR. The CO₂ gas is derived from pyrolysis of the ester group in the plasticizer, and the oxygen in both CO and

H₂O is derived from the ester group in the DOTP. CH₄ is a product of removing hydrogen chloride from polyvinyl chloride, and undecomposed DOTP and carbide are still present in the decomposition product. The P-SZD thermal degradation process is shown in Scheme 1:

Kinetic analysis

Nonisothermal thermal degradation

Due to the large change in chemical composition of polyvinyl chloride polymer materials, such as the addition of plasticizers, and stabilizers, a corresponding change in the thermal degradation of polyvinyl chloride results. In the inert gas state: polyvinyl chloride → pyrolysis → generation of volatiles + gas + carbide. The rate of the thermal decomposition reaction can usually be expressed by Eq. (1) [22]:

$$\frac{d\alpha}{dt} = A \exp\left(-\frac{E}{RT}\right) f(\alpha) \quad (1)$$

where α is the reaction fraction at t (min), $f(\alpha)$ is the reaction mechanism function and E is the activation energy (kJ mol⁻¹). A is the pre-exponential factor of Arrhenius (min⁻¹) and T is the absolute temperature (K). The thermal decomposition kinetics of the polymer were studied by mathematically transforming Eq. (1) and combining the TG thermogravimetric curve and the DTG curve. To avoid the calculation error caused by the different assumptions of the calculation method itself, this paper uses the Kissinger method [23], the Flynn–Wall–Ozaw (FWO) method [24, 25], the Friedman method [26] and the Kissinger–Akabira–Sunose (KAS) method [27]. The thermal decomposition kinetic parameters were calculated separately for the samples.

Kissinger method

$$\ln\left(\frac{\beta}{T_p^2}\right) = \ln\left(\frac{AR}{E}\right) - \frac{E}{RT_p} \quad (2)$$

In Eq. (2), β is the linear heating rate (°C/min), and T_p is the peak temperature of DTG at different heating rates. By creating a linear relationship curve of $\ln\left(\beta/T_p^2\right)$ versus $1/T_p$, and linearly fitting the data, the corresponding E and A can be obtained.

F–W–O method

$$\lg \beta = \lg\left(\frac{AE}{Rg(\alpha)}\right) - 2.315 - 0.4567 \frac{E}{RT} \quad (3)$$

Table 1 Composition of PVC blends

Sample	Dosage/g				
	PVC	DOTP	S	Z	D
Blank	100	50	0	0	0
P-S	100	50	1.0	0	0
P-SZ	100	50	0.5	0.5	0
P-SZD	100	50	0.5	0.5	1.0

P-SZD (solid) \rightarrow pyrolysis \rightarrow ($\text{CH}_4 + \text{HCl} + \text{CO}_2 + \text{H}_2\text{O}$, etc.) (volatile gas) + DOTP (liquid) + carbide containing tin and zinc

Scheme 1 Thermal degradation process of P-SZD

In Eq. (3), $g(\alpha)$ is an integral mechanism function describing the decomposition reaction; when α is constant, $g(\alpha)$ is also constant, then $\lg\beta$ is linear with $1/T$. From this, E corresponding to a certain α can be obtained

Friedman method

$$\ln\left(\beta \frac{d\alpha}{dT}\right) = \ln[Af(\alpha)] - \frac{E}{RT} \quad (4)$$

In Eq. (4), when α is a certain value that is plotted by $\ln(\beta d\alpha/dT)$ versus $1/T$, the linear fit gives a straight line, and the activation energy E of the sample can be obtained from the slope ($-E/R$)

KAS method

$$\ln\left(\frac{\beta}{T^2}\right) = \ln\left[\frac{AR}{g(\alpha)E}\right] - \frac{E}{RT} \quad (5)$$

In Eq. (5), $\ln(\beta/T^2)$ is used to curve $1/T$, and the data are linearly fitted to obtain the corresponding kinetic parameter E . None of the above methods involve errors in the calculation of kinetic parameters by the mechanism functions $f(\alpha)$ and $g(\alpha)$. At a fixed heating rate β , the reaction kinetic parameters E , A and the linear coefficient r can be calculated from the above linear relationship.

Generalized dynamic equations

The infinite temperature of the kinetic rate equation is defined by the introduction of the generalized time θ [28, 29], such as in Eq. (6), then:

$$\theta = \int_0^t \exp\left(-\frac{E}{RT}\right) dt \quad (6)$$

where θ means that when an infinite temperature is reached, a reaction time of a specific α is reached, and when Eq. (6) is differentiated, the following is obtained:

$$\frac{d\theta}{dt} = \exp\left(-\frac{E}{RT}\right) \quad (7)$$

Combined with Eqs. (1) and (7), Eq. (8) is obtained:

$$\frac{d\alpha}{d\theta} = Af(\alpha) \quad (8)$$

or

$$\frac{d\alpha}{d\theta} = \frac{d\alpha}{dt} \exp\left(\frac{E}{RT}\right) \quad (9)$$

In Eq. (9), $d\alpha/d\theta$ corresponds to the generalized reaction rate, obtained by inferring the real-time reaction rate $d\alpha/dt$ at infinite temperature, and the integral form of the kinetic rate equation Eq. (10) is obtained by Eq. (8)

$$g(\alpha) = \int_0^\alpha \frac{d\alpha}{f(\alpha)} = A \int_0^\theta d\theta = A\theta \quad (10)$$

Master plot based on the differential form of the generalized dynamic equation

Using the reference point of $\alpha = 0.5$, the following equation can be easily derived from Eq. (8):

$$\frac{d\alpha/d\theta}{(d\alpha/d\theta)_{\alpha=0.5}} = \frac{f(\alpha)}{f(0.5)} \quad (11)$$

In Eq. (11), $f(0.5)$ is a constant of a given kinetic model function, and this is indicated at a given α , when using an appropriate description of the process $f(\alpha)$. The algebraic expressions of the common mechanism functions $f(\alpha)$ and $g(\alpha)$ are shown in Table 2. The table mainly includes chemical reaction, random nuclear growth and two-dimensional and three-dimensional diffusion and other mechanism models [22, 30]. The experimentally determined value of the differential/generalized reaction rate, $(d\alpha/d\theta)/(d\alpha/d\theta)_{\alpha=0.5}$, is equivalent to the theoretically calculated value $f(\alpha)/f(0.5)$. Because the two values depend only on α , comparing the theoretical master plot of $(d\alpha/d\theta)/(d\alpha/d\theta)_{\alpha=0.5}$ for α and the theoretical master plot of $(d\alpha/d\theta)/(d\alpha/d\theta)_{\alpha=0.5}$ for α , and assuming that the various $f(\alpha)$ functions are plotted, the method is exactly the same as the traditional master plot. The theoretical master plot of all $f(\alpha)$ functions coincide at $\alpha = 0.5$ and diffuse significantly between different $f(\alpha)$ functions in the range of $\alpha < 0.5$. According to Eq. (9), the differential/generalized reaction rate has the following relationship with experimental kinetic data:

$$\frac{d\alpha/d\theta}{(d\alpha/d\theta)_{\alpha=0.5}} = \frac{d\alpha/dt}{(d\alpha/dt)_{\alpha=0.5}} \frac{\exp(E/RT)}{\exp(E/RT_{0.5})} \quad (12)$$

In Eq. (12), $T_{0.5}$ is a reaction temperature of $\alpha = 0.5$. To calculate the experimental value $(d\alpha/d\theta)/(d\alpha/d\theta)_{\alpha=0.5}$, experimental kinetic data must be considered for different temperature conditions. For experimental kinetic data under isothermal conditions, the exponential terms in

Table 2 Algebraic expressions for the $f(\alpha)$ and $g(\alpha)$ functions for the common mechanisms in solid-state reactions

Rate-determining mechanism	Symbol	$f(\alpha)$	$g(\alpha)$
Chemical reaction	F1.5	$2(1 - \alpha)^{3/2}$	$1/(1 - \alpha)^{1/2} - 1$
Chemical reaction	F2	$(1 - \alpha)^2$	$1/(1 - \alpha) - 1$
Chemical reaction	F3	$1/2(1 - \alpha)^3$	$1/(1 - \alpha)^2 - 1$
Assumed random nucleation and its subsequent growth, $n = 1$	F1	$1 - \alpha$	$-\ln(1 - \alpha)$
Assumed random nucleation and its subsequent growth, $n = 3/2$	A1.5	$3/2(1 - \alpha)[- \ln(1 - \alpha)]^{1/3}$	$[- \ln(1 - \alpha)]^{2/3}$
Assumed random nucleation and its subsequent growth, $n = 2$	A2	$2(1 - \alpha)[- \ln(1 - \alpha)]^{1/2}$	$[- \ln(1 - \alpha)]^{1/2}$
Assumed random nucleation and its subsequent growth, $n = 3$	A3	$3(1 - \alpha)[- \ln(1 - \alpha)]^{2/3}$	$[- \ln(1 - \alpha)]^{1/3}$
Two-dimensional diffusion	D2	$1/[- \ln(1 - \alpha)]$	$(1 - \alpha)\ln(1 - \alpha) + \alpha$
Three-dimensional diffusion, spherical symmetry	D3	$3/2(1 - \alpha)^{2/3}[1 - (1 - \alpha)^{1/3}]^{-1}$	$[1 - (1 - \alpha)^{1/3}]^2$
Three-dimensional diffusion, cylindrical symmetry	D4	$3/2[1 - (1 - \alpha)^{1/3}]^{-1}$	$1 - 2\alpha/3 - (1 - \alpha)^{2/3}$
Contracting cylinder (cylindrical symmetry)	R2	$2(1 - \alpha)^{1/2}$	$1 - (1 - \alpha)^{1/2}$
Contracting sphere (spherical symmetry)	R3	$3(1 - \alpha)^{2/3}$	$1 - (1 - \alpha)^{1/3}$

Eq. (12) cancel each other out due to $T = T_{0.5}$, so that the experimental master plot can be obtained directly from an isotherm curve of $d\alpha/dt$ versus α . On the other hand, for all nonisothermal data, the exponential term in Eq. (12) cannot be eliminated. To calculate the differential/generalized reaction rate for a given isothermal data under linear and nonlinear heating, in addition to the individual measured kinetic data, the E value of this process is known. As a special case of nonlinear nonisothermal data, the real-time ratio of the rate term in Eq. (12) is the uniformity of the kinetic data of the CRTA.

Main master plot based on the integral form of kinetic data

From the integral form to the infinite temperature integral dynamics equation Eq. (10), the following equation can be obtained using the reference point at $\alpha = 0.5$:

$$\frac{g(\alpha)}{g(0.5)} = \frac{\theta}{\theta_{0.5}} \quad (13)$$

In Eq. (13), $\theta_{0.5}$ is the generalized time, based on the differential master plot of Eq. (11) and the integral method by infinite temperature. It can be constructed by comparing various theoretical master plots of the differential/generalized time $\theta/\theta_{0.5}$ for α and $g(\alpha)/g(0.5)$ for α . The theoretical master plot of various $g(\alpha)$ functions overlaps with $g(\alpha)/g(0.5) = 1$ when $\alpha = 0$, $g(\alpha)/g(0.5) = 0$ and $\alpha = 0.5$. However, assuming different $g(\alpha)$ functions, in the range of $\alpha > 0.5$, there is a significant difference. The theoretical master plots of different kinetic models have significant differences in the range of values of α . For the differential master plot and the integral master plot, $\alpha < 0.5$ and $\alpha > 0.5$, respectively. By following these two master plot methods, it is possible to verify the dynamic consistency

with a particular kinetic model function throughout the process. According to the kinetic data under isothermal conditions, Eq. (6) can be expressed as:

$$\theta = \exp\left(-\frac{E}{RT}\right)t \quad (14)$$

Since the exponential term in Eq. (14) is a constant during the reaction, the value of $\theta/\theta_{0.5}$ at a given α is equal to $t/t_{0.5}$, then Eq. (13) is converted to

$$\frac{g(\alpha)}{g(0.5)} = \frac{t}{t_{0.5}} \quad (15)$$

Equation (15) is the same as the master plot of kinetic data under isothermal conditions. Therefore, an alpha isothermal kinetic curve for (t) is sufficient to calculate the experimental master of $\theta/\theta_{0.5}$ for α . Under nonisothermal conditions, solving the integral defined in Eq. (6) requires an understanding of the temperature dependence on time.

From the dynamic data at the linear heating rate of β , the value of θ given by α can be calculated by Eq. (16):

$$\theta = \frac{1}{\beta} \int_0^T \exp\left(-\frac{E}{RT}\right) dT = \frac{E}{\beta R} \int_x^\infty \frac{\exp(-x)}{x^2} dx = \frac{E}{\beta R} p(x) \quad (16)$$

Here, $x = E/RT$, and the function $p(x)$ cannot be represented in closed form, although there are several convergence levels in its approximation, as the fourth reasonable approximation has been reported in the recent literature [31, 32], making $E/RT = 20$ more than $10^{-5}\%$, such as Eq. (17):

$$p(x) = \frac{e^{-x}}{x} \pi(x) \quad (17)$$

and Eq. (18):

$$\pi(x) = \frac{x^3 + 18x^2 + 86x + 96}{x^4 + 20x^3 + 120x^2 + 240x + 120} \tag{18}$$

For a linear heating rate, the value of $\theta/\theta_{0.5}$ can be calculated from Eq. (19):

$$\frac{\theta}{\theta_{0.5}} = \frac{p(x)}{p(x_{0.5})} \tag{19}$$

To calculate the experimental data obtained from a linear heating program, the experimental master plot of $\theta/\theta_{0.5}$ versus α requires a known α as a function of temperature and an E value.

Master plot based on the integral form and differential form of the kinetic equation

Multiplying the differential form Eq. (8) by the integral kinetic equation, Eq. (10) gives the following expression for the kinetic equation at infinite temperature:

$$\theta \frac{d\alpha}{d\theta} = f(\alpha)g(\alpha) \tag{20}$$

The values of $\theta(d\alpha/d\theta)$ and $f(\alpha)g(\alpha)$ in Eq. (20) depend only on α , and according to Eqs. (9), (16)–(18), experimental curves are available. Based on Eq. (20), various kinetic model functions $\theta(d\alpha/d\theta)$ versus α experimental master plot are assumed. This can be compared with the theoretical master plot of $f(\alpha)g(\alpha)$ versus α .

Results and discussion

Thermal behavior of different samples

Table 3 shows the characteristic parameters of thermal degradation of different samples, and it can be seen from the table that when the conversion rate α is 5% and 70%, the decomposition temperature is from high to low as P-SZD > P-S > P-SZ, and as the conversion rate is 85%, the decomposition temperature is P-SZ > P-SZD > P-S.

Figure 1 shows the TG–DTG curves for different samples when the heating rate is $10 \text{ }^\circ\text{C min}^{-1}$ under a nitrogen atmosphere and heating to $200.5 \text{ }^\circ\text{C}$. The conversion rates of P-S, P-SZ and P-ZSD were 0.72, 0.49 and 0.71%,

respectively. When heated to $700 \text{ }^\circ\text{C}$, the corresponding gas and evaporate conversion rates were 93.2, 88.9 and 88.3%, respectively, and the corresponding carbide residues were 6.81, 11.02 and 10.42%, respectively. After adding 0.33% by mass of zinc stearate, the gasification rate decreased by 4.30%. With the addition of 1.0 phr of dipentaerythritol, the residual carbide was almost unchanged. It can be seen that the addition of organic additives does not change the final conversion rate of thermal degradation.

It can be seen from the small box in Fig. 1a that after adding Z and D, if the temperature is lower than $228.6 \text{ }^\circ\text{C}$, the conversion rate of P-SZ ($\alpha < 2\%$) is smaller than P-S. Similarly, if the temperature is lower than $252.6 \text{ }^\circ\text{C}$, the conversion rate of P-SZD ($\alpha < 5.4\%$) is also smaller than P-S. When the temperature is higher than $332.4 \text{ }^\circ\text{C}$, the conversion rate of P-ZSD ($\alpha > 68.4\%$) < P-SZ < P-S. Similarly, if the temperature is higher than $337.9 \text{ }^\circ\text{C}$, the conversion rate of P-ZS ($\alpha > 70.4\%$) < P-S.

If the temperature is higher than $433 \text{ }^\circ\text{C}$, curves b and c almost overlap, and the interaction of D with the film almost disappears. However, in the interval of $332 \sim 700 \text{ }^\circ\text{C}$, the difference in thermogravimetry between curves b, c and curve a is obvious; at this point, 0.5 phr of Z was added, and the thermal degradation of the film is remarkable, which inhibits further degradation of the film. This may be due to the incomplete decomposition of stearic acid in Z and the result of Zn(II) and hydrogen chloride to form ZnCl_2 .

It can be seen from curves a, b and c in Fig. 1b that the maximum decomposition rate of P-SZ and P-SZD samples after addition of Z and D is significantly lower than that of P-S at approximately $300 \text{ }^\circ\text{C}$. Since the peak temperatures of curves b and c almost overlap, this indicates that only Z suppresses the rate of thermal degradation of the film, that is, zinc stearate inhibits the rate of hydrogen chloride formation, and the addition of D does not change the decomposition rate of the film, so D does not function with hydrogen chloride.

Table 3 Characteristic parameters of thermal degradation of different samples

Sample	$T_{5\%}/^\circ\text{C}$	$T_{10\%}/^\circ\text{C}$	$T_{30\%}/^\circ\text{C}$	$T_{50\%}/^\circ\text{C}$	$T_{70\%}/^\circ\text{C}$	$T_{85\%}/^\circ\text{C}$	$T_{p1}/^\circ\text{C}$	$T_{p2}/^\circ\text{C}$	*Residue/%
P-S	251.0	267.5	296.0	306.5	336.0	455.1	301.4	457.5	6.81
P-SZ	245.0	259.7	286.4	302.3	332.6	475.8	298.7	456.6	11.02
P-SZD	251.7	262.7	287.6	302.6	350.3	474.8	297.7	454.0	10.42

$T_{5, 10, 30, 50, 70, 90\%}$ are the temperatures at which the decomposition rates are 5, 10, 30, 50, 70 and 90%, respectively; T_{p1} and T_{p2} are the peak temperatures at the first and second stage of the DTG curves, respectively; * at $700 \text{ }^\circ\text{C}$

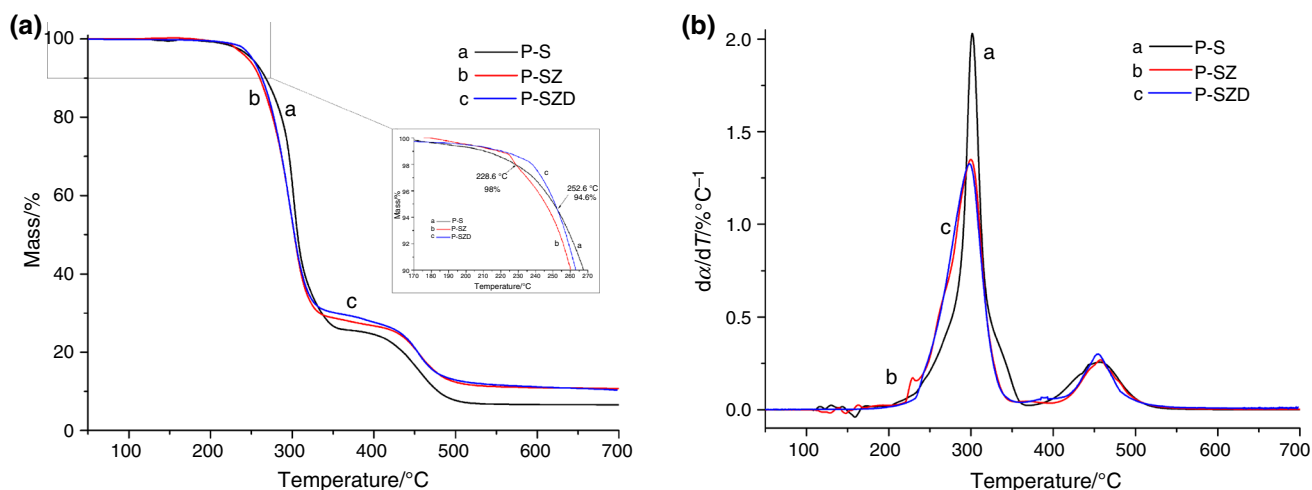


Fig. 1 TG–DTG curves of different samples. (Note: **a** P-S; **b** P-SZ; **c** P-SZD)

TG–IR analysis

At a heating rate of $10\text{ }^{\circ}\text{C min}^{-1}$ and under a high-purity argon atmosphere, the gas phase 3D TG–FTIR spectrum of P-SZD and blank sample pyrolysis is shown in Fig. 2. As seen from the figure, the infrared peak height and position of the blank and P-SZD are significantly different.

Figure 2a is a TG–IR perspective view of a blank sample. When heated to $275\text{ }^{\circ}\text{C}$, the wavenumbers of the released gas are 1101 , 1264 and 1736 cm^{-1} all due to the vibration peak of the ester group $\nu_{(\text{COOR})}$ in the plasticizer. The vibration peak located near 1508 cm^{-1} is due to the $\nu_{(\text{aromatic ring})}$. The vibration peak located in the range of $3500\sim 3900\text{ cm}^{-1}$ is due to the hydroxyl $\nu_{(\text{OH})}$. If heated to $300\text{ }^{\circ}\text{C}$, the peak belongs to the $\nu_{(\text{CO}_2)}$ vibration peak

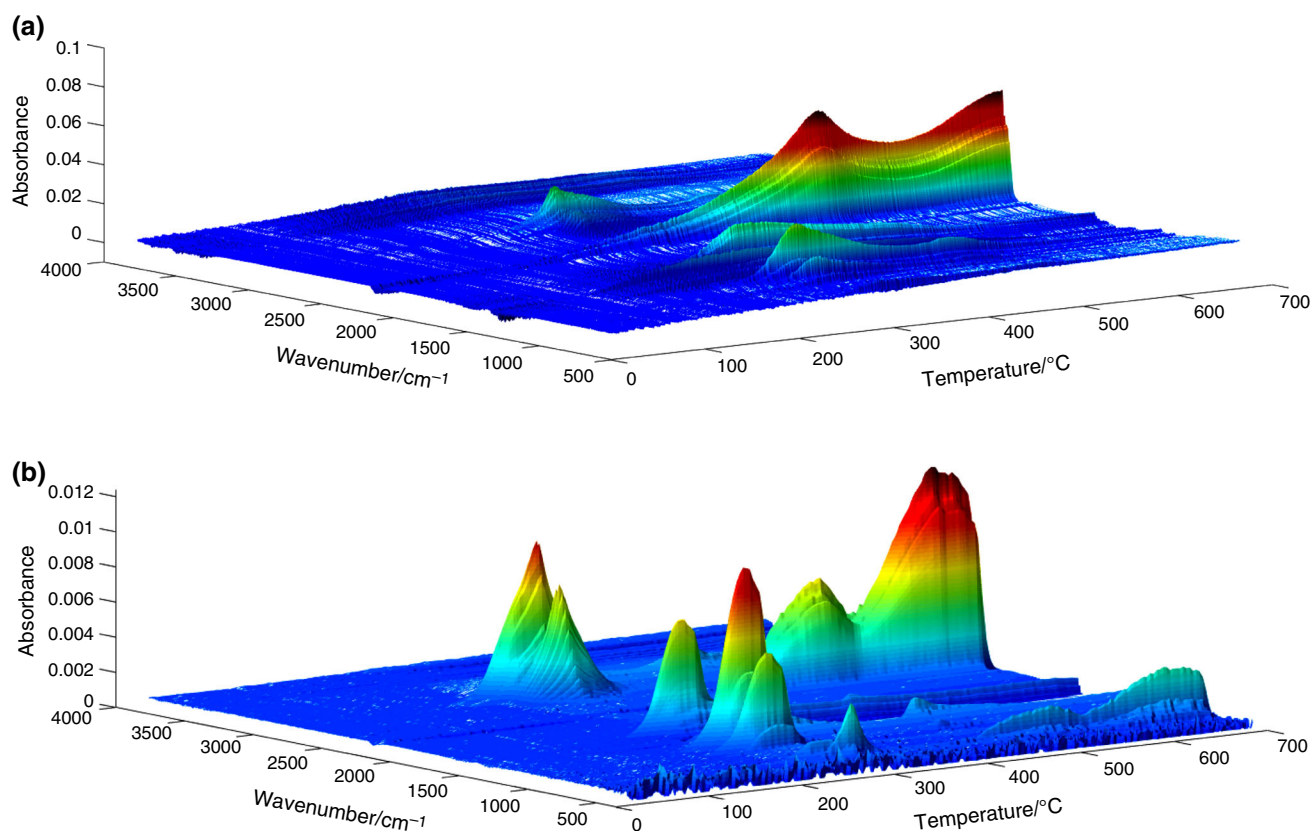


Fig. 2 3D TG–FTIR spectrum of gas phase in the thermal degradation of **a** blank and **b** P-SZD

near 669 cm^{-1} and to the vibration peak of hydrogen chloride $\nu_{(\text{HCl})}$ near 2966 cm^{-1} . If heated to $318\text{ }^\circ\text{C}$, it is attributed to $\nu_{(\text{HCl})}$ vibration approximately 2962 cm^{-1} . After continued heating to $324\text{ }^\circ\text{C}$ and near 728 cm^{-1} , a small amount of acetylene gas $\nu_{(-\text{C}\equiv\text{C}-)}$ is formed [33]. At $469\text{ }^\circ\text{C}$ and $505\text{ }^\circ\text{C}$, the 2278 and 2361 cm^{-1} vibration peaks that appear, respectively, are due to the $\nu_{(\text{CO}_2)}$ group. It can be seen that gases with different wavenumbers and characteristic groups are released at different temperatures [34, 35]. The vibration peaks from strong to weak are: ν_{CO_2} ($505\text{ }^\circ\text{C}$) > ν_{HCl} ($318\text{ }^\circ\text{C}$) > $\nu_{(-\text{COOR})}$ ($324\text{ }^\circ\text{C}$) > $\nu_{(\text{aromatic ring})}$ ($275\text{ }^\circ\text{C}$).

Figure 2b is a TG–IR stereogram of P-SZD. If the decomposition peak temperature is near $275\text{ }^\circ\text{C}$, the vibration peaks corresponding to the wavenumbers approximately 1100 , 1264 and 1738 cm^{-1} are all due to the plasticizer ester group $\nu_{(-\text{COOR})}$. In the interval of $3500\sim 3900\text{ cm}^{-1}$, no hydroxyl $\nu_{(-\text{OH})}$ vibration peak is generated. In addition, if heated to $300\text{ }^\circ\text{C}$, the wavenumbers 2798 and 2962 cm^{-1} belong to the hydrogen chloride gas $\nu_{(\text{HCl})}$ vibration peak.

When the temperature is $299\text{ }^\circ\text{C}$ and $635\text{ }^\circ\text{C}$, or $515\text{ }^\circ\text{C}$ and $638\text{ }^\circ\text{C}$, the corresponding vibration peaks are 672 , 2358 and 2310 cm^{-1} , respectively, and they all belong to the $\nu_{(\text{CO}_2)}$ group. It can be seen that gases of corresponding different characteristic groups are released at different temperatures [34, 35]. The vibration peaks from strong to weak are: ν_{CO_2} ($638\text{ }^\circ\text{C}$) > $\nu_{(-\text{COOR})}$ ($275\text{ }^\circ\text{C}$) > ν_{HCl} ($299\text{ }^\circ\text{C}$).

Figure 3 is an infrared spectra of the released gas at different temperatures, wherein the black curve represents a blank and the red curve represents P-SZD. Figure 3a–g is wavenumber/Abs infrared spectra at temperatures of 275 , 300 , 350 , 400 , 500 and $635\text{ }^\circ\text{C}$, respectively. As the pyrolysis temperature proceeds at a heating rate of $10\text{ }^\circ\text{C min}^{-1}$, when slowly rising from 275 to $635\text{ }^\circ\text{C}$, the vibration peak in the range of $2358\sim 2362\text{ cm}^{-1}$ is attributed to CO_2 , and the intensity in the blank sample continues to increase. In contrast, P-SZD generates a weaker vibration peak near $640\text{ }^\circ\text{C}$. Almost no CO_2 is produced; in other words, CO_2 gas is suppressed during thermal degradation and is less likely to overflow.

Figure 4 shows the relative intensity curves of the P-SZD and blank release gases (CH_4 , H_2O , CO_2 and CO) as determined by TG–IR. Figure 4a shows the gas released during thermal degradation of the blank sample. The peak intensity from strong to weak is: $\text{CO}_2 > \text{CH}_4 > \text{H}_2\text{O} > \text{CO}$. Among them, CO_2 generates a double-headed peak maximum near $500\text{ }^\circ\text{C}$ and $700\text{ }^\circ\text{C}$, respectively. The methane overflows approximately $310\text{ }^\circ\text{C}$ and $480\text{ }^\circ\text{C}$, and the water overflows in the range of $130\text{--}600\text{ }^\circ\text{C}$ and generates a small amount of CO . Figure 4b shows the gas released by thermal degradation of P-SZD, and the peak

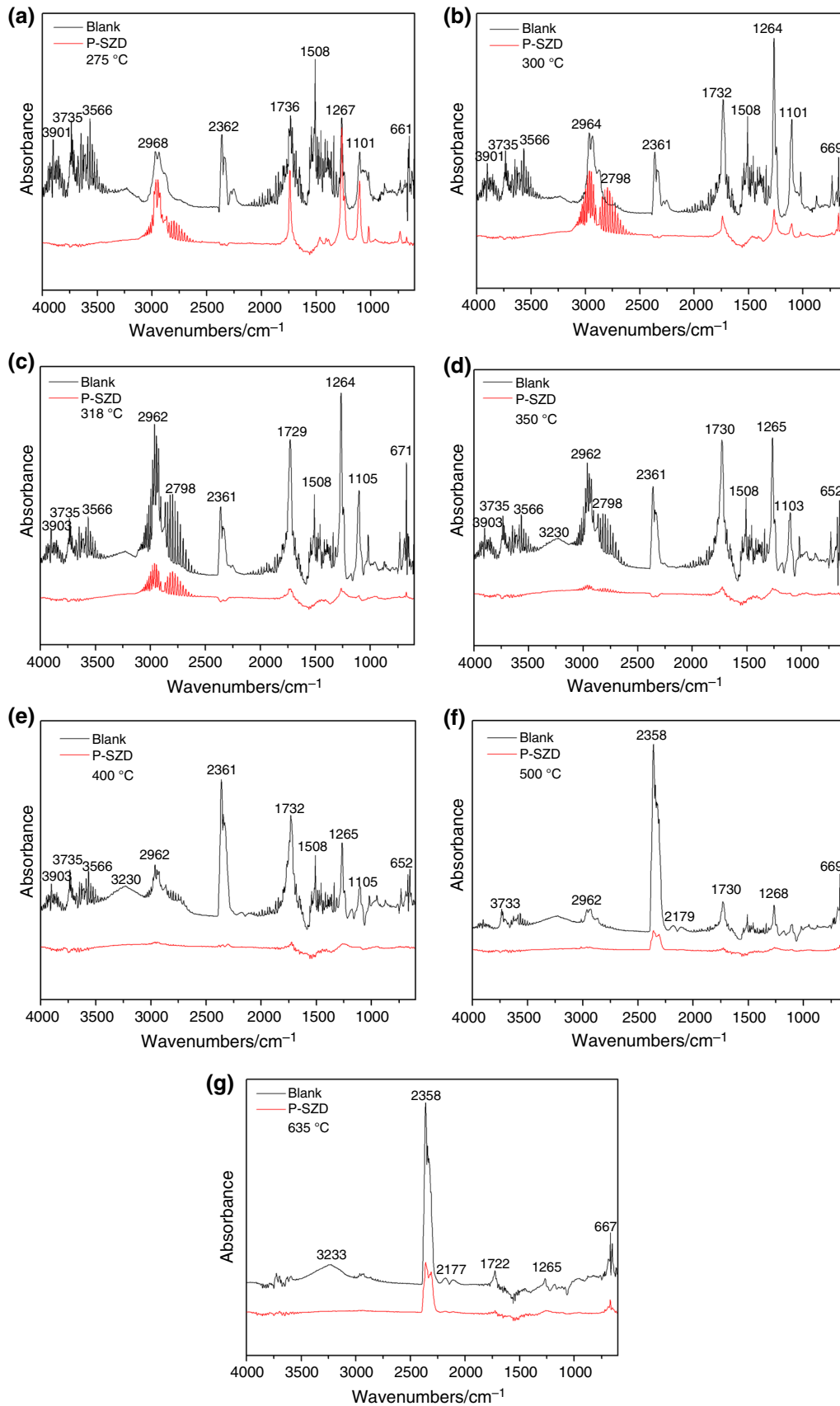
Fig. 3 Infrared spectrum of gas released at different pyrolysis temperatures. (Note: **a** $275\text{ }^\circ\text{C}$; **b** $300\text{ }^\circ\text{C}$; **c** $318\text{ }^\circ\text{C}$; **d** $350\text{ }^\circ\text{C}$; **e** $400\text{ }^\circ\text{C}$; **f** $500\text{ }^\circ\text{C}$; **g** $635\text{ }^\circ\text{C}$)

intensity from strong to weak is: $\text{CH}_4 > \text{CO}_2 > \text{CO} > \text{H}_2\text{O}$, where methane is released at approximately $300\text{ }^\circ\text{C}$ and $460\text{ }^\circ\text{C}$, CO_2 is released in the range of $560\sim 700\text{ }^\circ\text{C}$, and the peak near $500\text{ }^\circ\text{C}$ is disappeared compared with the blank sample. Furthermore, a maximum is formed near $640\text{ }^\circ\text{C}$, and the strength is reduced by 85.2% . However, the release of methane gas is similar in intensity, the release of H_2O in the blank is significantly higher than that in P-SZD, and the latter does not see water overflow. It can be seen from the figure that after adding the auxiliary P-SZD, (S), (Z) and (D) to the polyvinyl chloride film significantly inhibited the decarboxylation of DOTP so that the amount of CO_2 gas released is significantly lower than that of the blank. This may be due to the strong interaction of Sn, Zn and hydroxyl groups with the ester group. There is the possibility of generating a relatively stable carboxyl group-containing metal complex, and this facilitates the recycling of the plasticizer DOTP.

Nonisothermal kinetics

Under a nitrogen atmosphere and at a heating rate of 2.5 , 5 , 10 and $20\text{ }^\circ\text{C min}$, the TG and DTG curves for P-SZD pyrolysis were generated and are shown in Fig. 5. As seen from the figure, thermal degradation is divided into two stages, and the first and second stage pyrolysis intervals are $200\sim 375\text{ }^\circ\text{C}$ and $375\sim 550\text{ }^\circ\text{C}$, respectively. Table 4 is a characteristic parameter of thermal degradation of P-SZD, where $T_{1\%}$ and $T_{5\%}$ are the temperatures at which the decomposition rates are 1% and 5% , respectively. T_{p1} and T_{p2} are the peak temperatures of the first and second stages on the DTG ($\%/^\circ\text{C}$) curve, respectively. T_{2on} is the initial temperature of the second stage decomposition. $M1$ and $M2$ ($d\alpha/dT$) are the maximum decomposition rates of the first and second stages, respectively, when the heating rate is increased from 2.5 to $20\text{ }^\circ\text{C min}^{-1}$. The temperatures at the conversion rate of 1% were 190.6 , 222.9 , 227.7 and $232.4\text{ }^\circ\text{C}$. If β is $2.5\text{ }^\circ\text{C min}^{-1}$, the peak temperatures of T_{p1} and T_{p2} were $276.0\text{ }^\circ\text{C}$ and $433.9\text{ }^\circ\text{C}$, respectively.

Figure 6 is a linear relationship curve of P-SZD pyrolysis based on different methods. Figure 6a–d are linear relationship curves based on Eq. (2) the $\ln\beta/T_{p2}$ versus $1/T_p$ for Kissinger method, Eq. (3) the $\ln\beta$ versus $1/T$ for FWO method, Eq. (4) the $\ln(\beta d\alpha/dT)$ versus $1/T$ for Friedman method and Eq. (5) $\ln\beta/T^2$ versus $1/T$ for KAS method. As can be seen from the figure, the linear relationship is better than previous methods. The kinetic parameters, apparent activation energy E and pre-exponential factor A of P-SZD thermal degradation were obtained by a nonisothermal



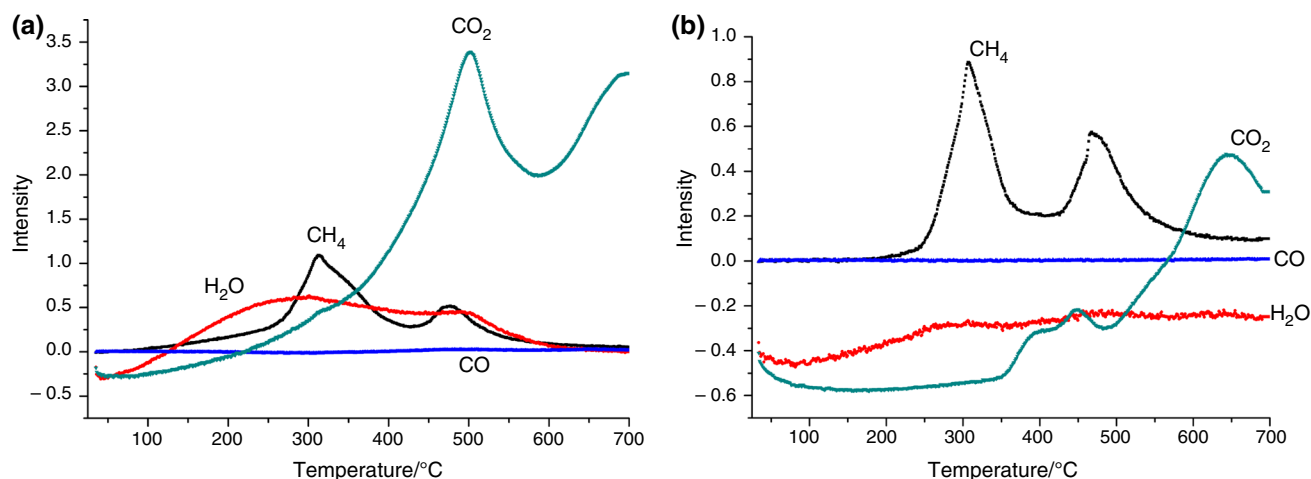


Fig. 4 Gas formation rates analyzed by TG-FTIR. (Note: **a** P-SZD; **b** blank; Heating rate both are $10\text{ }^{\circ}\text{C min}^{-1}$; Argon atmosphere)

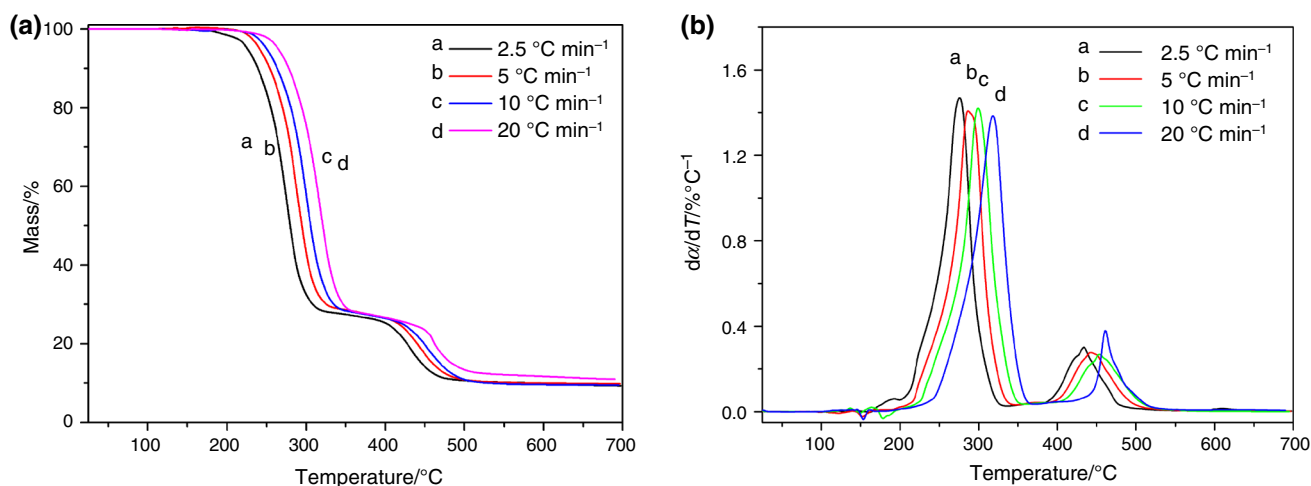


Fig. 5 TG and DTG curves of P-SZD

Table 4 Characteristic parameters of thermal degradation of P-SZD

$\beta/\text{ }^{\circ}\text{C min}^{-1}$	$T_{1\%}/^{\circ}\text{C}$	$T_{5\%}/^{\circ}\text{C}$	$T_{p1}/^{\circ}\text{C}$	$T_{2on}/^{\circ}\text{C}$	$T_{p2}/^{\circ}\text{C}$	$M_1/\% \text{ }^{\circ}\text{C}^{-1}$	$M_2/\% \text{ }^{\circ}\text{C}^{-1}$	*Residue/%
2.5	190.6	226.1	276.0	373.9	433.9	1.469	0.311	9.43
5.0	222.9	241.3	286.7	385.7	442.8	1.407	0.276	9.84
10	227.7	250.3	299.9	392.2	453.8	1.421	0.268	9.47
20	232.4	264.9	318.2	411.3	461.5	1.385	0.380	11.21

$T_{1\%}$ and $T_{5\%}$ are the temperatures at which the decomposition rates are 1% and 5%, respectively; T_{p1} and T_{p2} are the peak temperatures of the first and second stages on the DTG curve, respectively; T_{2on} is the initial temperature of the second stage thermal decomposition; M_1 and M_2 ($d\alpha/dT$) are the maximum decomposition rates of the first and second stages, respectively; * at $650\text{ }^{\circ}\text{C}$

model-free method the FWO method, the Friedman method and the KAS method, as shown in Table 5, where E is the apparent activation energy, r is the linear coefficient and SD is the standard deviation. As shown in Fig. 6a, for the kinetic parameters solved by the Kissinger method in

Eq. (2) in the first and second stages, the apparent activation energies E obtained were 114.0 and 298.9 kJ mol^{-1} , respectively. The pre-exponential factors $\ln A$ obtained were 17.36 and 43.21 min^{-1} , respectively. The linear coefficients r obtained were 0.9930 and 0.9975 ,

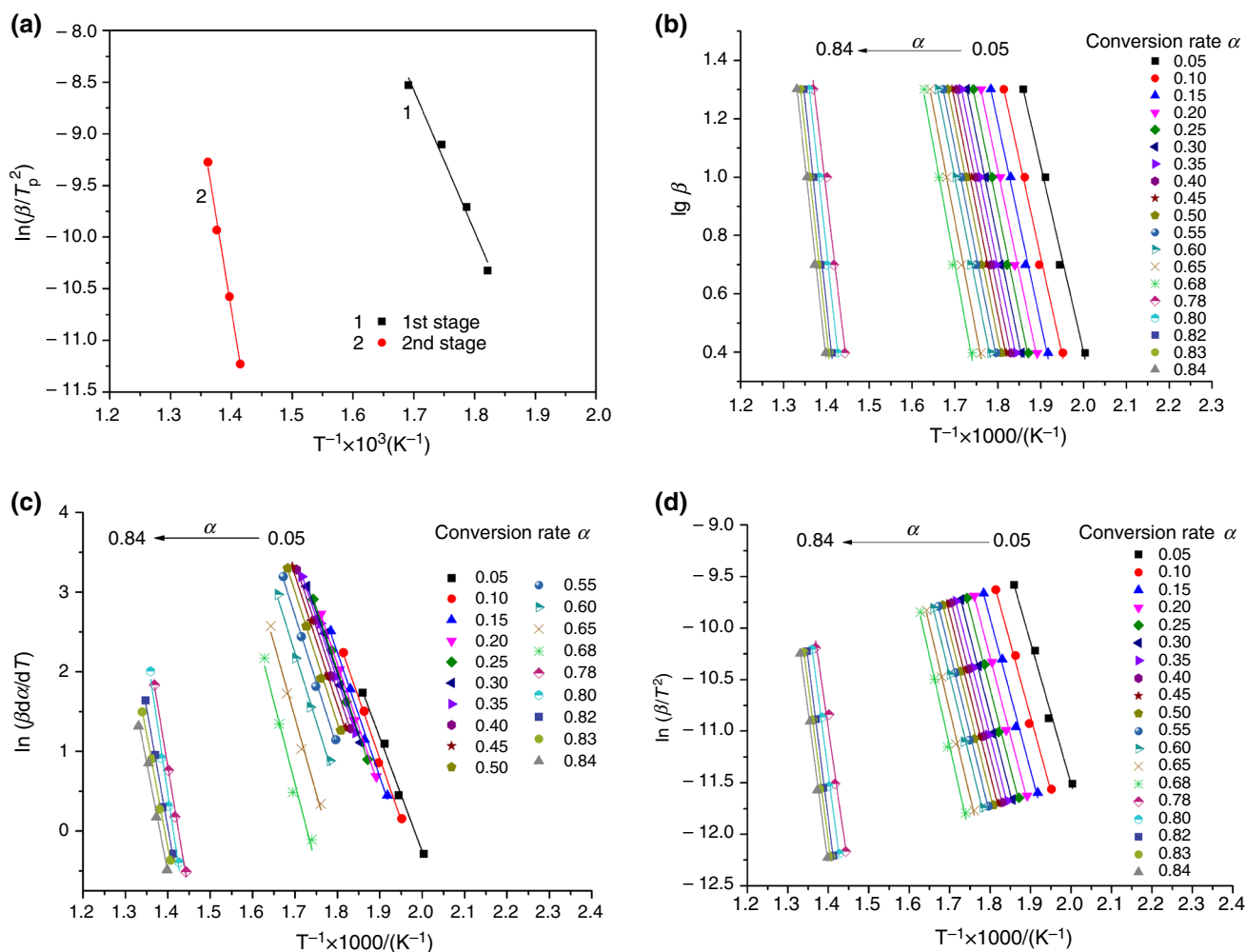


Fig. 6 Linear relationship curve of different methods of pyrolysis. (Note: **a** $\ln \beta/T_p^2 \sim 1/T_p$ (Kissinger); **b** $\ln \beta \sim 1/T$ (FWO); **c** $\ln (\beta d\alpha/dT) \sim 1/T$ (Friedman); **d** $\ln \beta/T_p^2 \sim 1/T$ (KAS))

respectively, and the standard deviation SD was 0.1120 and 0.0733, respectively.

It can be seen from Table 5 that the conversion range in the first stage is 0.05–0.68, and the minimum and maximum activation energies of the FWO method are 116.3 and 147.4 kJ mol^{-1} , respectively. In the second stage, the conversion rate ranged from 0.78 to 0.84, and the activation energy minimum and maximum were 226.3 and 247.8 kJ mol^{-1} , respectively, the activation energy increased slowly. In the first stage, the average apparent activation energies E calculated according to the FWO method, the Friedman method and the KAS method were 131.0, 136.5 and 128.5 kJ mol^{-1} , respectively. The average apparent activation energies E of the second stage solution were 245.8, 255.4 and 246.5 kJ mol^{-1} , respectively.

Figure 7 is a functional dependence of the conversion rate α and the apparent activation energy E_a for different methods. It can be seen from the figure that when the

conversion rate is in the range of 0.05–0.65, the apparent activation energy is approximately constant, and the activation energy solved by the Friedman method is slightly increased, and the activation energy obtained by the FWO and KAS methods is similar. This indicates that there is a possibility of the same reaction mechanism in this interval. When the conversion rate increases to 0.65–0.85, the activation energy increases sharply, which indicates that the reaction is complicated and the reaction mechanism changes. At this time, the reaction must be performed at a higher temperature. As seen from Table 5, the average apparent activation energies E solved in the first and second stages were 127.5 and 261.6 kJ mol^{-1} , respectively.

Thermal degradation mechanism

Substituting the first stage $E = 127.5 \text{ kJ mol}^{-1}$ and the second stage $E = 249.2 \text{ kJ mol}^{-1}$ into the generalized kinetic equation, we obtained the theoretical master plot

Table 5 Kinetic parameters solved by different methods

Stage	α	FWO			Friedman			KAS		
		r	SD	E/kJ mol ⁻¹	r	SD	E/kJ mol ⁻¹	r	SD	E/kJ mol ⁻¹
1st	0.05	0.9949	0.0479	116.3	0.9967	0.0865	118.8	0.9942	0.1100	113.6
	0.10	0.9960	0.0426	121.3	0.9969	0.0853	127.2	0.9954	0.0978	118.7
	0.15	0.9966	0.0393	125.1	0.9976	0.0756	129.8	0.9961	0.0900	122.6
	0.20	0.9971	0.0362	127.7	0.9983	0.0630	131.1	0.9967	0.0829	125.2
	0.25	0.9976	0.0327	129.6	0.9989	0.0500	131.5	0.9973	0.0750	127.0
	0.30	0.9980	0.0298	130.4	0.9984	0.0586	129.3	0.9978	0.0683	127.8
	0.35	0.9983	0.0276	130.4	0.9977	0.0701	129.9	0.9981	0.0633	127.8
	0.40	0.9983	0.0282	131.0	0.9972	0.0797	132.9	0.9980	0.0648	128.3
	0.45	0.9980	0.0299	132.0	0.9970	0.0824	135.2	0.9977	0.0686	129.3
	0.50	0.9980	0.0303	133.0	0.9978	0.0715	136.7	0.9977	0.0695	130.4
	0.55	0.9981	0.0290	134.3	0.9982	0.0637	138.2	0.9979	0.0666	131.6
	0.60	0.9983	0.0276	135.7	0.9973	0.0808	141.9	0.9981	0.0632	133.1
	0.65	0.9982	0.0288	140.3	0.9953	0.1139	157.1	0.9979	0.0657	137.8
	0.68	0.9968	0.0382	147.4	0.9879	0.1900	171.4	0.9964	0.0875	145.2
Mean						136.5			128.5	
2nd	0.78	0.9915	0.0620	226.3	0.9981	0.0749	266.1	0.9906	0.1430	226.1
	0.80	0.9970	0.0368	249.1	0.9934	0.1428	296.7	0.9967	0.0848	250.0
	0.82	0.9971	0.0365	254.9	0.9949	0.1032	248.5	0.9968	0.0838	256.0
	0.83	0.9972	0.0356	250.9	0.9972	0.0741	236.8	0.9969	0.0818	251.7
	0.84	0.9975	0.0338	247.8	0.9932	0.1125	228.8	0.9972	0.0777	248.4
Mean			245.8			255.4			246.5	

E apparent activation energy, r linear coefficient, SD standard deviation

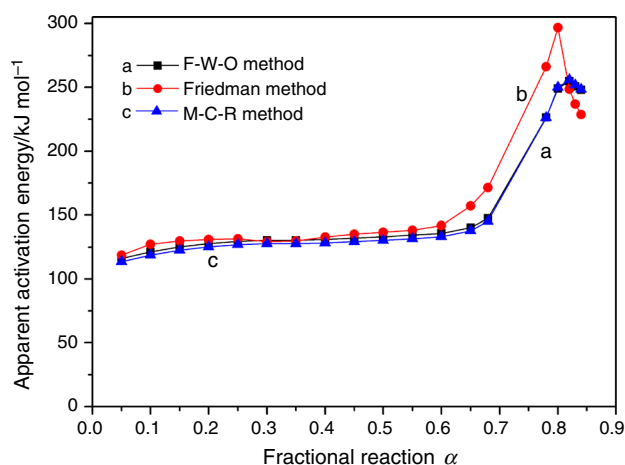


Fig. 7 Functional dependence of equal conversion rate α and apparent activation energy E

and the experimental master plot curves, as shown in Fig. 8. The theoretical master plots are F1, R2, R3, A2, D2, F1.5, F2 and F3.

Figure 8 is the relationship curve for $\theta/\theta_{0.5}$ versus α . The experimental data points obtained according to Eq. (15)

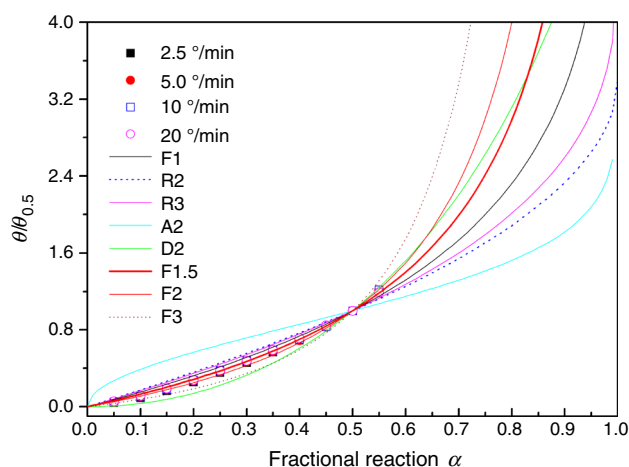


Fig. 8 Comparison between theoretical master plots generated from kinetic model in Table 1 and the generalized master plots generated from experimental curves

fall on the theoretical master plot F1.5 response curve obtained by Eq. (13), and the overlap is consistent with the chemical reaction F1.5 mechanism model. Figure 9 depicts the simulated and experimental α vs T curves obtained for P-SZD. Overall the simulated curves were in good

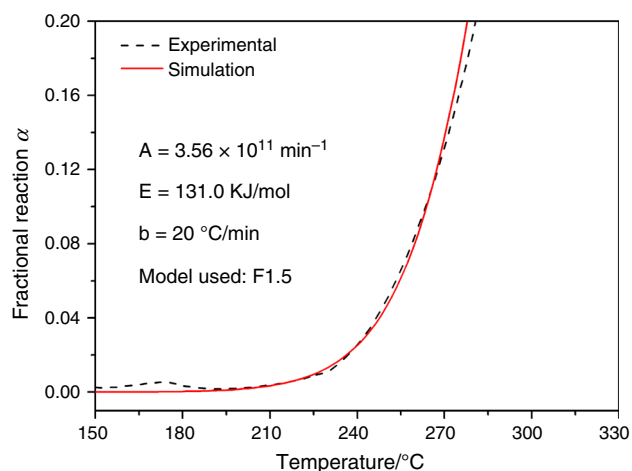


Fig. 9 Simulation of P-SZD thermal decomposition using kinetic data obtained from FWO method and reaction mechanism obtained from master plots

agreement with the experimental results, which infers that the identified kinetic parameters were accurate. Matching between simulated and experimental values was very good in the low conversion range, where the conversion rate better conformed to conditions of kinetic control, and in particular the modeled α versus T curve for P-SZD at 20 °C min^{-1} superimposed the experimental curve for all conversions below 0.2.

As seen from the figure, the experimental data with a heating rate of 20 °C min^{-1} is the closest to the F1.5 reaction model. It can be seen from the above that P-SZD has a decomposition rate of $0.05\sim 0.20$, and the thermal decomposition reaction and the chemical reaction 1.5-order theoretical curve almost overlap. It conforms to the chemical reaction 1.5-order mechanism model, and its differential mechanism function $f(\alpha) = 2(1 - \alpha)^{3/2}$, and the integral mechanism function is $g(\alpha) = 1/(1 - \alpha)^{1/2} - 1$.

Conclusions

Polyvinyl chloride films containing the mercaptan methyltin(S), zinc stearate (Z) and dipentaerythritol (D) additives were prepared, and the thermal degradation kinetics of P-SZD films were investigated using TG-DTG and TG-FTIR techniques. The results show that when the heating rates are 2.5, 5.0, 10 and 20 °C min^{-1} , the lowest temperatures at the conversion rates of 5 and 10% are 226.1 and 239.1 °C, respectively. The average apparent activation energies of the film in the first and second stages using the Kissinger method, the Friedman method, the KAS method and the FWO method obtained are 127.5 and 261.6 kJ mol^{-1} , respectively.

By comparing the generalized master plot with the experimental master plot, we found that on the master plot of $\theta/\theta_{0.5}$ versus α , the thermal degradation conforms to the F1.5 reaction mechanism model of a chemical reaction. The differential mechanism function $f(\alpha)$ is $2(1 - \alpha)^{3/2}$, and the integral mechanism function $g(\alpha)$ is $1/(1 - \alpha)^{1/2} - 1$.

TG-FTIR analysis showed that the gas components released by thermal degradation of P-SZD film were mainly methane, CO_2 , water and trace CO. The 3D TG-IR diagram of the blank and P-SZD was significantly different. As the heating progresses (the heating rate is 10 °C min^{-1}), the temperature rises slowly from 275 to 635 °C, and the CO_2 vibration peak appears in the range of $2358\sim 2362\text{ cm}^{-1}$, the intensity of the blank vibration peak continues to increase, while the P-SZD sample has almost no CO_2 vibration peak except in the vicinity of 640 °C. The vibration peaks from strong to weak are: ν_{CO_2} (638 °C) $>$ $\nu_{(-\text{COOR})}$ (275 °C) $>$ ν_{HCl} (299 °C). The thermal degradation of P-SZD showed no hydroxyl or water formation compared with the blank. The CO_2 gas released from the P-SZD thermal degradation had a maximum near 640 °C, while the CO_2 released by the blank produced double peaks at 500 and 700 °C. The relative intensity of the degradation is 6.0 times higher than that of P-SZD.

It can be seen that adding SZD to the polyvinyl chloride film significantly inhibited the removal of carboxyl groups in the DOTP molecule, which reduced the release of CO_2 gas by 85.2%. This may be due to Sn, Zn and hydroxyl groups interacting strongly with ester groups in DOTP, and there is the potential to generate a more stable carboxyl-containing metal complex to create conditions for the recovery and recycling of DOTP.

Acknowledgements Financial support from the National Natural Science Foundation of China (Grant Number: 21775002) are gratefully acknowledged.

References

- Hahladakis JN, Velis CA, Weber R, Iacovidou E, Purnell P. An overview of chemical additives present in plastics: migration, release, fate and environmental impact during their use, disposal and recycling. *J Hazard Mater.* 2018;344:179–99.
- Yu J, Sun LS, Ma C, Qiao Y, Yao H. Thermal degradation of PVC: a review. *Waste Manag.* 2016;48:300–14.
- Castro A, Soares D, Vilarinho C. Kinetics of thermal de-chlorination of PVC under pyrolytic conditions. *Waste Manag.* 2012;32:847–51.
- Zhu HM, Jiang XG, Yan JH, Chi Y, Cen KF. TG-FTIR analysis of PVC thermal degradation and HCl removal. *J Anal Appl Pyrol.* 2008;82:1–9.
- Xu FF, Wang B, Yang D, Hao JH, Qiao YY, Tian YY. Thermal degradation of typical plastics under high heating rate conditions by TG-FTIR: pyrolysis behaviors and kinetic analysis. *Energy Convers Manag.* 2018;171:1106–15.

6. Cao QM, Yuan GA, Yin LJ, Chen DZ, He PJ, Wang H. Morphological characteristics of polyvinyl chloride (PVC) dechlorination during pyrolysis process: influence of PVC content and heating rate. *Waste Manag.* 2016;58:241–9.
7. Honus S, Kumagai S, Fedorko G, Molnár V, Yoshioka T. Pyrolysis gases produced from individual and mixed PE, PP, PS, PVC, and PET—part I: production and physical properties. *Fuel.* 2018;221:346–60.
8. Sadat-Shojai M, Bakhshandeh GR. Recycling of PVC wastes. *Polym Degrad Stab.* 2011;96:404–15.
9. Wu JL, Chen TJ, Luo XT, Han DZ, Wang ZQ, Wu JH. TG/FTIR analysis on co-pyrolysis behavior of PE, PVC and PS. *Waste Manag.* 2014;34:676–82.
10. Beneš M, Milanov N, Matuschek G, Kettrup A, Plaček V, Balek V. Thermal degradation of PVC cable insulation studied by simultaneous TG–FTIR and TG–EGA methods. *J Therm Anal Calorim.* 2004;78:621–30.
11. Jackić M, Vrandečić NS, Erceg M. Kinetic analysis of the non-isothermal degradation of poly(vinyl chloride)/poly(ethylene oxide) blends. *J Therm Anal Calorim.* 2016;123:1513–22.
12. Krongauz VV, Lee YP, Bourassa A. Kinetics of thermal degradation of poly(vinyl chloride). *J Therm Anal Calorim.* 2011;106:139–49.
13. Beneš M, Plaček V, Matuschek G, Kettrup AA, Györyová K, Emmerich WD, Balek V. Lifetime simulation and thermal characterization of PVC cable insulation materials. *J Therm Anal Calorim.* 2005;82:761–8.
14. Sánchez-Jiménez PE, Perejón A, Criado JM, Diánez MJ, Pérez-Maqueda LA. Kinetic model for thermal dehydrochlorination of poly(vinyl chloride). *Polymer.* 2010;51:3998–4007.
15. Wang YL, Wang XY, Liu LM, Peng XY. Theoretical study on the thermal dehydrochlorination of model compounds for poly(vinyl chloride). *J Mol Struct Theochem.* 2009;896:34–7.
16. Ludwig V, Da Costaludwig ZM, Rodrigues MM, Anjos V, Costa CB, Sant’ Anna das Dores DR, da Silva VR, Soares F. Analysis by Raman and infrared spectroscopy combined with theoretical studies on the identification of plasticizer in PVC films. *Vib Spectrosc.* 2018;98:134–8.
17. Fang YQ, Wang QW, Guo CG, Song YM, Cooper PA. Effect of zinc borate and wood flour on thermal degradation and fire retardancy of Polyvinyl chloride (PVC) composites. *J Anal Appl Pyrol.* 2013;100:230–6.
18. Mohamed NA. Biologically active maleimido aromatic 1,3,4-oxadiazole derivatives evaluated thermogravimetrically as stabilizers for rigid PVC. *J Therm Anal Calorim.* 2018;131:2535–46.
19. Wang CJ, Liu HR, Zhang JQ, Yang SL, Zhang Z, Zhao WP. Thermal degradation of flame-retarded high-voltage cable sheath and insulation via TG–FTIR. *J Anal Appl Pyrol.* 2018;134:167–75.
20. Lu YH, Liu WL, Wei F, Ma SC. Effect of barium stearate on the thermal stability of polyvinyl chloride. *Appl Mech Mater.* 2013;395–396:371–6.
21. Wei F, Lu YH, Liu WL. Effect of organotin on the thermal stability of poly(vinyl chloride). *Adv Mater Res.* 2012;550–553:838–42.
22. Vyazovkin S, Burnham AK, Criado JM, Pérez-Maqueda LA, Popescu C, Sbirrazzuoli N. ICTAC Kinetics Committee recommendations for performing kinetic computations on thermal analysis data. *Thermochim Acta.* 2011;520(1–2):1–19.
23. Kissinger HE. Reaction kinetics in differential thermal analysis. *Anal Chem.* 1957;29(11):1702–6.
24. Ozawa T. A new method of analyzing thermogravimetric data. *Bull Chem Soc Jpn.* 1965;38(11):1881–6.
25. Flynn JH, Wall LA. General treatment of the thermogravimetry of polymers. *J Res Natl Bur Stand.* 1966;70(6):487–523.
26. Friedman HL. Kinetics of thermal degradation of char-forming plastics from thermogravimetry. Application to a phenolic plastic. *J Polym Sci Polym Symp.* 1964;6(1):183–95.
27. Akahira T, Sunose T. Method of determining activation deterioration constant of electrical insulating materials. *Res Rep Chiba Inst Technol (Sci Technol).* 1971;16:22–31.
28. Gotor FJ, Criado JM, Malek J, Koga N. Kinetic analysis of solid-state reactions: the universality of master plots for analyzing isothermal and nonisothermal experiments. *J Phys Chem A.* 2000;104(46):10777–82.
29. Sánchez-Jiménez PE, Pérez-Maqueda LA, Perejón A, Criado JM. Generalized master plots: a straightforward approach for determining the kinetic model: the case of cellulose pyrolysis. *Thermochim Acta.* 2013;552:54–9.
30. Turmanova SC, Genieva SD, Dimitrova AS, Vlaev LT. Non-isothermal degradation kinetics of filled with rice husk ash polypropylene composites. *Express Polym Lett.* 2008;2(2):133–46.
31. Senum GI, Yang RT. Rational approximations of the integral of the Arrhenius function. *J Therm Anal.* 1977;11:445.
32. Flynn JH. The ‘temperature integral’-its use and abuse. *Thermochim Acta.* 1997;300:83–92.
33. Fazekas P, Czégény Z, Mink J, Bódis E, Klébert S, Németh C, Keszler AM, Károly Z, Szépvölgyi J. Decomposition of poly(vinyl chloride) in inductively coupled radiofrequency thermal plasma. *Chem Eng J.* 2016;302:163–71.
34. Jia PY, Hu LH, Zhang M, Zhou YH. TG–FTIR and TG–MS analysis applied to study the flame retardancy of PVC–castor oil-based chlorinated phosphate ester blends. *J Therm Anal Calorim.* 2016;124:1331–9.
35. Qi YX, Wu WH, Han LJ, Qu HQ, Han X, Wang AQ, Xu JZ. Using TG–FTIR and XPS to understand thermal degradation and flame-retardant mechanism of flexible poly(vinyl chloride) filled with metallic ferrites. *J Therm Anal Calorim.* 2016;123:1263–71.

Publisher’s Note Springer Nature remains neutral with regard to jurisdictional claims in published maps and institutional affiliations.